Supplementary Information

Self-Powered Ice Growth Sensing System for Transmission Lines Based on Triboelectric Nanogenerator and Micro Thermoelectric Generator

Yingli Lu [a,1], *Changxin Liu* [a,1,*], *Yi Wang* [a], *Zhiije Hao, Chutian Chen* [b], *Bo Dong* [b], *Xun Zhou* [c]

[a] Marine Engineering College, Dalian Maritime University, Dalian 116000, Dalian, PR China

[b] Key Laboratory of Ocean Energy Utilization and Energy Conservation of Ministry of Education, School of Energy and Power Engineering, Dalian University of Technology, Dalian, 116024, PR China

[c] School of Vehicle and Transport Engineering, Henan University of Science and Technology, Luoyang 471003, China.

E-mail: liu_changxin@dlmu.edu.cn (C.X. Liu)

(1: These authors contributed equally to this work.)

Files include:

Supporting Note S1: Morphology of AAO template and PR/PDMS material

In this study, anodic aluminum oxide (AAO) served as the template and was integrated with polydimethylsiloxane (PDMS) and chitosan to formulate a composite material designated as PR/PDMS. To gain a comprehensive understanding of the morphological and structural characteristics of both the AAO template and the PR/PDMS composite, scanning electron microscopy (SEM) was employed for their detailed characterization.

AAO templates are extensively utilized in the synthesis of diverse nanomaterials owing to their distinctive porous architecture. In the present study, we utilized the AAO template supplied by the manufacturer and incorporated its SEM image, depicted in Fig. S1(a), to illustrate its native morphology. The SEM image reveals that the AAO template possesses a highly organized porous structure, with pores uniformly distributed and possessing uniform diameters. This characteristic provides an exemplary templating effect for subsequent experiments. Consequently, the AAO template offers a notable advantage in the fabrication of nanomaterials with specific morphologies and structures.

In this study, PR/PDMS, a novel composite material, is employed as the friction layer of the sensor. To investigate its morphological structure, we conducted scanning SEM analysis on its cross-section, with the results presented in Fig. S1(b). The SEM image clearly reveals the presence of numerous irregular pore structures and air pockets within the PR/PDMS. These structural characteristics impart a notable porous architecture to the PR/PDMS. The existence of these porous structures not only enhances the surface roughness of the PR/PDMS but also affords it a greater number of active sites and a higher specific surface area.

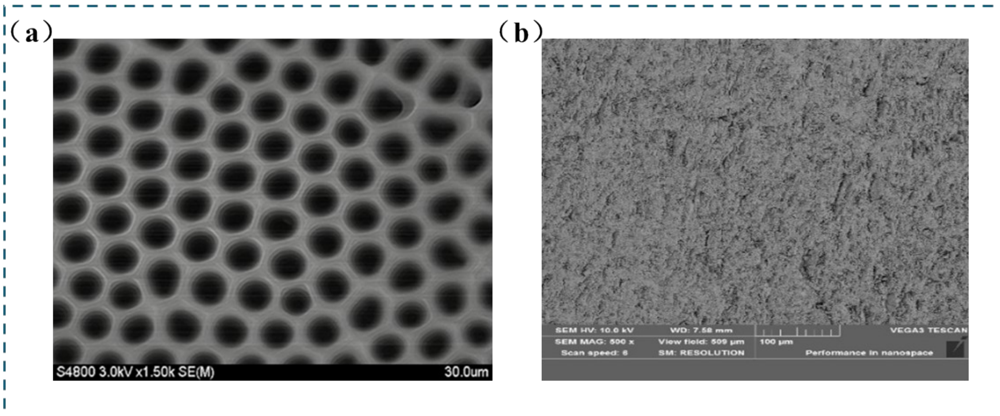

Fig. S1. (a) SEM image of AAO template (b) SEM image of PR/PDMS

Further analysis indicates that the porous structure of PR/PDMS is likely intimately associated with the incorporation of chitosan and the utilization of an AAO template during processing. The incorporation of chitosan may have modified the cross-linking density and network configuration of PDMS, leading to the generation of an increased number of pores and air pockets. Conversely, the porous structure of the AAO template served as an optimal templating agent for the fabrication of PR/PDMS. This templating effect enabled PR/PDMS to replicate the pore architecture of the AAO template, thereby exhibiting a comparable porous morphology.

Supporting Note S2: Multichannel signal acquisition process and design

The response of the HP-TENG array to localized ice thickness was evaluated using a multi-channel measurement system (National Instruments). The aluminum (Al) electrodes of all HP-TENG units were connected via conductive wires, while the copper (Cu) electrodes of each channel were linked to the probes of the corresponding measurement channels. A voltmeter with an internal resistance of approximately 10 MΩ was used as the measuring instrument, recording voltage peaks that corresponded to the localized thickness response of each TENG unit in the array. When one-third of the channels (CH1-CH2) were simultaneously compressed, voltage peaks were observed exclusively at CH1 and CH2, whereas the output curves of the remaining channels remained nearly constant during the same period.

The principle of the multichannel signal acquisition circuit is shown in Figure S2.

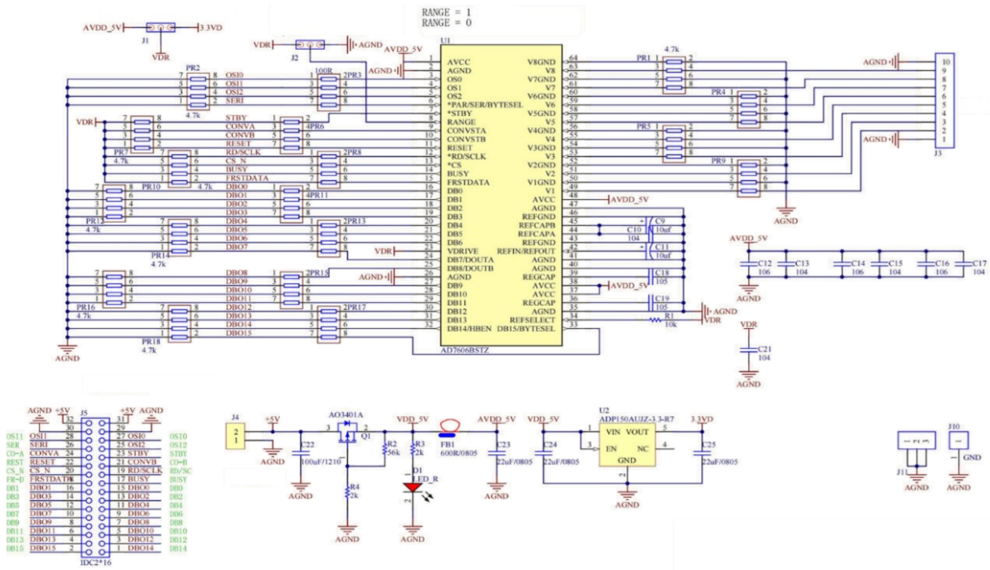

Fig. S2. Schematic diagram of a multi-channel signal acquisition circuit

The multi-channel signal management circuits incorporate a 2.5V bandgap voltage reference and a reference buffer circuit with a typical temperature coefficient of ±10 ppm/°C. The selection of an internal or external reference depends on the specific system requirements. For applications requiring high absolute accuracy in multichip ADC designs, an external reference with superior initial accuracy and a low-temperature coefficient is recommended to mitigate errors arising from discrepancies between the internal references of different devices. In this study, the ADR421B, offering an initial accuracy of 0.04% and a temperature coefficient of 3 ppm/°C, is utilized.

For scenarios demanding precise numerical matching across channels in multichip ADCs, a hybrid approach can be employed. The first multichannel signal management circuit operates in internal reference mode, while the remaining circuits are configured to use external reference mode. The built-in reference output of the first circuit is then supplied to the remaining circuits. This configuration ensures channel-to-channel data consistency across multiple multichannel signal management circuits without requiring an additional external reference. However, the overall system's absolute accuracy is ultimately determined by the performance of the built-in reference.

The digital interface of the multi-channel signal management circuit supports both parallel and serial configurations. With a Vdrive ranging from 2.3V to 5.25V, it is compatible with the most modern CPUs and DSPs. Notably, when operating in serial interface mode, the DB [15:9] and DB [6:0] pins of the data bus must be grounded to ensure proper functionality.

The multi-channel signal management circuit incorporates oversampling and digital filtering capabilities. The oversampling ratio (OSR) can be configured as x2, x4, x8, x16, x32, or x64 using the OS[2:0] pins. When oversampling is activated, the internal oversampling control circuit and a first-order Sinc digital filter are automatically engaged, adjusting the -3 dB bandwidth accordingly.

Analog-to-digital converters (ADCs) typically require both analog and digital power supplies. While most systems provide a 5V digital power supply, a corresponding 5V analog power supply may not always be available. In such cases, if the analog and digital circuits share the same 5V power source, undesirable digital noise may couple into the analog circuit, impairing the ADC's performance. To minimize this risk, this design approach is generally discouraged. However, if sharing the power supply is unavoidable, the 5V digital power supply must be thoroughly filtered before being used by the analog circuit. The decoupling design for the multi-channel signal management circuit is straightforward, requiring only nine capacitors, two 10 μF, two 1 μF, and five 0.1 μF, as illustrated in Figure S3.

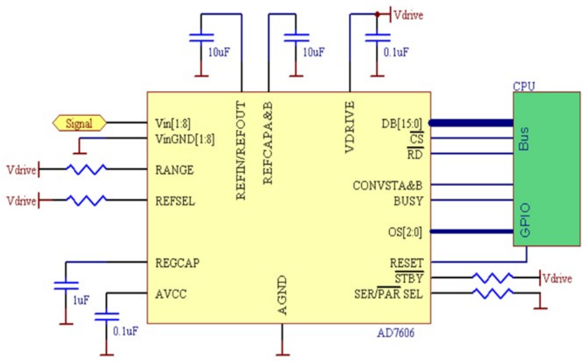

Fig.S3. peripheral circuit design

Supporting Note S3: Effect of the surface potential barrier of the triboelectric material on the output performance of the MP-TENG

In the contact-separation mode of the triboelectric nanogenerator (TENG), the metal layer encounters the polydimethylsiloxane (PDMS) layer via an externally applied downward force. As the rigid metal layer exerts pressure, the protruding surface structure of the PDMS undergoes deformation until an equilibrium is established between the repulsive force of the PDMS and the downward force of the metal. Under identical downward forces, the dome-shaped surface structure deforms more significantly than the cylindrical surface structure, owing to the cylindrical structure's higher repulsive force compared to the dome-shaped structure. Consequently, the effective contact area between the metal surface and the PDMS differs in these two scenarios. The structure experiencing greater deformation results in an increased charge density on the material's surface. The variations in surface structure and surface charge density between these two cases influence the sensitivity and durability of the TENG, as illustrated in Figure S4.

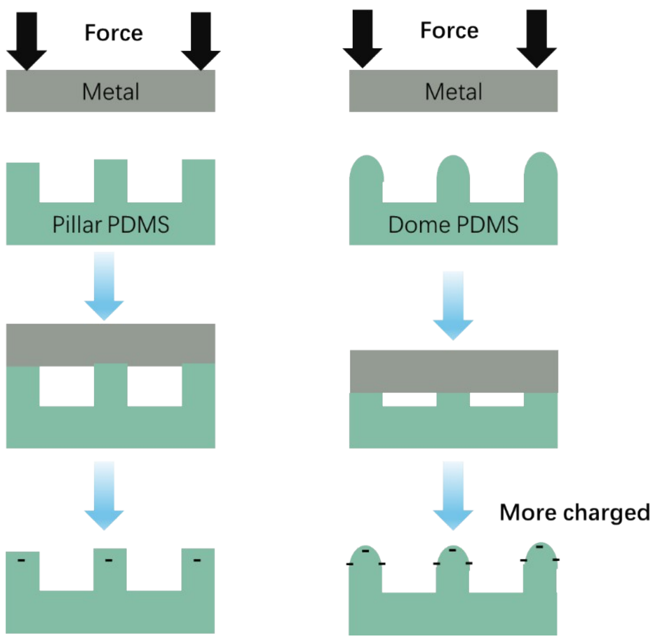

Figure S4: Effect of protruding surface shapes on the performance of the friction layer in contact-separation mode

The discrepancy arises due to the regulation of the potential barrier that electronic transmission must traverse by distinct contact materials. The work function, or contact potential difference, between these two materials influences the propensity and direction of electron transfer from one material to the other. The surface morphology of dome-like protrusions serves to augment the contact area, resulting in the formation of numerous micro-capacitors. These micro-capacitors enhance the surface charge density within the friction layer, ultimately leading to an improvement in the electrical output of triboelectric nanogenerators (TENGs). As illustrated in Supplementary Figures S2 and S3, the electrical output performance of Dome PDMS surpasses that of Pillar PDMS, and both exhibit superior performance compared to Bare PDMS.

Supporting Note S4: Detailed derivation of the theoretical MTEG model

The relationship between the surface temperature of overhead transmission lines composed of steel-core aluminum conductors (ACSR) and the current can be derived by considering the resistive heating and heat dissipation of the conductors. Here is a simplified derivation process, assuming that the conductor is uniform and neglecting some complex factors like radiation losses. First, the resistive heating power of the conductor can be calculated using the following formula:

$$P_r = I^2 R \#(1)$$

Where P_r is the resistive heating power, I is the current carrying capacity of the transmission line, and R is the resistance of the conductor. Next, we can consider the heat dissipation of the wire. The surface temperature of the wire $T_{surface}$, the ambient temperature $T_{ambient}$, the length of the wire L, and the cross-sectional area of the wire A. According to the heat transfer equation, we can obtain the following relationship:

$$P_d = \frac{kA\left(T_{surface} - T_{ambient}\right)}{L} \#(2)$$

Where P_d represents the power dissipated by thermal conduction in the transmission line.

At thermal equilibrium, the resistive heating power equals the dissipation power:

$$T_{surface} = \frac{I^2 RL}{KA} + T_{ambient} \#(3)$$

Therefore, with an increase in the current-carrying capacity of the transmission line, the resistive heating power increases, consequently leading to an elevation in surface temperature.

The working principle of the MTEG is the Seebeck effect. When the transmission line is carrying a normal current, the surface temperature of the transmission line T_h remains consistently higher than the ambient temperature T_c, creating a temperature gradient ΔT (i.e., $T_h > T_c$) between the contact points of the conductor material. Subsequently, holes in the p-type semiconductor and electrons in the n-type semiconductor begin to diffuse and accumulate at the high and low-temperature ends, thereby generating an electromotive force ΔU in the circuit.

The magnitude of ΔU is directly proportional to ΔT, with the proportionality coefficient being the Seebeck coefficient. Its expression is as follows:

$$\alpha = lim_{\Delta T \to 0}\frac{\Delta U}{\Delta T} = \frac{dU}{dT}\#(4)$$

The Seebeck electromotive force V_O in the circuit is:

$$V_O = \alpha\left(T_h - T_c\right)\#(5)$$

A portion of this voltage is applied to the internal resistance R of the thermocouple, while the other part is added to the load resistance R_L. The actual output voltage of the thermocouple is the voltage applied to the load resistance, and it can be expressed as follows:

$$V = \alpha \cdot \frac{I^2RL}{KA} \cdot \frac{R_L}{R_L + R}\#(6)$$

Table.S1 Letter abbreviation and symbol table

Letter abbreviation symbol	**Representative meaning**	**Unit**
ε_0	The vacuum permittivity	F / m
ε_1	The relative permittivity of Al	F / m
ε_2	The relative permittivity of PDMS	F / m

$x_1(t)$	The temporal variation in ice coating thickness	mm
$x_2(t)$	The deformation of PDMS	mm
Δx	The distance between the two electrodes	mm
Q	Electrodynamics	μC
Q_{sc}	The transfer of charge	μC
k_1	The elastic coefficient of spring	N/m
k_2	The elastic coefficient of PDMS	N/m
S	The area of the material	mm^2
$\Delta\sigma$	The change in the density of transferred charges	$\mu C / mm^2$
F	The spring force	N
P	The pressure on the PDMS layer	KPa
d_1	The initial spacing between PDMS and MTEG	mm
d_2	The thickness of PDMS	mm
C	Capacitance in PDMS	μF
E	The electric field strength in PDMS	V/m
α	Seebeck coefficient	$\mu V / K$
η	The efficiency of thermoelectric conversion	mW
ΔT	The temperature difference between the two ends	℃
T_h	The temperature of the high-temperature end	℃
T_c	The temperature of the low-temperature end	℃
$T_{ambient}$	The ambient temperature	℃
ZT	The thermoelectric figure of merit	/
κ	The total thermal conductivity of the material	W/(m • k)
K	The thermal conductivity	W/(m • k)

A	The cross-sectional area of the transmission line	mm^2
R	The conductor resistance	Ω
R_L	The load resistance	Ω
I	The current flowing through the transmission line	A
σ	Electrical conductivity	S/m

Table.S2 The equipment utilized in the experiment and its accuracy

Experimental instrument	**model**	**precision**	**Manufacturers**
Multi-channel data acquisition device	GM10	±0.3%	YOKOGAWA
Micro-nano material deposition inkjet printing	n.jet lab	1um	Notion
X-ray Diffraction	D8 QUEST	0.005°	Bruker
DC power source	PS-3010	0.5%	HUABAI
Laser Thermal Conductivity Analyzer	NanoTR	1%	Netzsch
Highly Accurate Seebeck Systems Number Tester	CTA-3	±7%	CRYALL